Preliminary Analysis of Visual Navigation Performance in Close Formation Flying

Renato Volpe
Dept.Mech.Aero.Eng.
University of Rome La Sapienza
Via Salaria 851, Rome, Italy
renatovolpe.92@gmail.com

Giovanni B. Palmerini
Scuola di Ingegneria Aerospaziale
University of Rome La Sapienza
Via Salaria 851, Rome, Italy
giovanni.palmerini@uniroma1.it

Christian Circi
Dept.Astro.Elec.Energ.Eng.
University of Rome La Sapienza
Via Salaria 851, Rome, Italy
christian.circi@uniroma1.it

Abstract—Growing interest has been lately put into proximity operations with non-cooperative targets, such as on-orbit servicing and refuelling, which both requires the the system to be completely autonomous. Autonomy is achieved through a robust GNC structure and the navigation system is of primary importance for this purpose. The paper investigates a scenario where a spacecraft (chaser) approaches a target satellite on an elliptical, sun-synchronous orbit. The approach maneuver itself is designed to be both optimal in time/propellant consumption, by means of solution of an inverse optimization problem, and safe, i.e. in such a way that no collision can exist between the chaser and the target. An optical navigation technique which relies both on optical camera and LIDAR measurements would provide the benefits of having more accurate measures and the possibility of assessing the targets shape and status, in case of them being unknown. The measurements' covariance for this navigation systems varies along the maneuver depending on several factors, as the chaser-target line of sight and the target illumination. As navigation and guidance are strictly connected, a change in the measurements' covariance modifies the maneuver's performance and can suggest a complete redesign of the docking. The paper, on the basis of reasonable assumptions for hardware characteristics, provides a preliminary analysis of the relevance of this coupling effect when considering variations in visibility conditions.

TABLE OF CONTENTS

1. INTRODUCTION

Nowadays, autonomous formation flying, rendezvous and docking can enable new solutions for space systems designers in various scenarios such as on-orbit servicing and refuelling, debris removal, satellite inspection, multi-docking operations, unknown celestial bodies exploration. Space systems autonomy can allow greater survivability when more than one spacecraft are in close proximity to each other, when the transmission delay is too long for ground control to take crucial decisions, when the communication bandwidth is too small to transmit all relevant informations to ground control and when failures occur. Moreover, as too large control networks should be required to continuously monitor the operations, space autonomy can make the system affordable in terms of costs and availability of ground based resource.

Above all, proximity operations with non-cooperative targets, which are substantially referred to as out-of-control, freely tumbling bodies, require that the system is able to make vital decisions, i.e. can react to contingencies, in a safe time frame and without errors, which can be achieved by excluding the human decision-making component.

The focus of this article is put on the operational aspect of the formation flight problem. We assume that the aim of the mission is to make some operations, such as refuelling or inspection, on a non-cooperative target in an elliptical sun-synchronous orbit. We then have a spacecraft, the chaser, which, departing from certain initial values with respect to the target, has to maneuver in order to dock with the target and be able to make the required operations.

In order to fulfill the required tasks, a robust Guidance, Navigation and Control (GNC) behaviour has to be designed in order to achieve the desired amount of autonomy. We would like to design a trajectory which is both optimal in terms of propellant's mass consumption and safe, i.e. excludes possible collisions between the chaser and the target. Then, we want to make the chaser follow that trajectory as closely as possible. Sensors are needed to acquire the measures and a filter is used to process them in order to obtain a state estimation, which can be used to compute the closed loop control required to follow the desired trajectory.

Two specific sensors are used in this simulation: a passive Camera and an active LIDAR. These sensors are used in real operations [1], [2] and provide a suitable solution for the close navigation phase. Their measurements noise, i.e. the measure's covariance, is often considered as constant throughout the entire maneuver. It is however reasonable to think that the performances of these sensors strongly depend either on the sunlight illumination of the target in the case of a passive sensor such as a camera, or on the angle of observation with respect to the target's surface normal in the case of an active sensor such as a LIDAR.

The intent of this research is to specifically study the impact of the variable performance of the sensors in a close formation flying, with the final goal to identify if and how the optimal trajectory selection will be affected. Indeed, different test cases will be analyzed to investigate how the sensors' performance degradation affects the overall maneuver performance, i.e. the estimation covariances and the Δv.

Several test cases will be analyzed to study how the sensor's performance degradation affects the overall maneuver performance, i.e. the estimation covariances and the Δv.

The feasibility of the maneuver will be assessed in the presence of target's eclipse periods, where no camera measurements can be obtained as the target is not detectable in

1

the visible spectrum. A solution to this problem will be presented by providing the spacecraft with an infrared sensor, able to take measurements when the target spacecraft is not illuminated.

The study is developed by means of numerical simulations obtained by a purposefully designed code. Even if a number of experimental tests have been and are currently carried on for related problems [3], [4], [5], it has been deemed that only a virtual scenario could enable a meaningful analysis of different light/geometry effects.

2. MANEUVER'S TEST CASES

The identification of an optimal guidance strategy for the docking to a non cooperative tumbling target can be faced by means of the approach already discussed in [6]. Indeed, we briefly recall here how the desired trajectory to be followed by the chaser is computed.

Given an initial relative state vector, a final docking point, the maneuver time and the spinning vector of the target spacecraft, an optimal docking trajectory in terms of Δv consumption can be computed by solving an inverse optimization problem. The strategy adopted is to parameterize the trajectory's 3D component by mean of polynomial expressions. The grade of the polynomials as to be chosen such as part of the constants are used to analytically satisfy the initial and final constraints, i.e. initial and final relative position and velocity, while the remaining are varied till a minimum of a specific cost function, i.e. the maneuver Δv, is localized.

In [6] the maneuver time has been varied for a fixed initial and final relative configuration and the optimal Δv has been computed in each case. Among all of them, there is a minimum Δv for a certain maneuver time. After several test cases analysis it has been found that the minimum Δv is obtained for a maneuver time equal to 0.9 times the target's orbital period. This is qualitatively explainable if we think that the free-dynamic relative trajectory in the Hill frame is usually a spiral around the target, which iteratively repeats roughly every target's orbital period. In order to consume as less propellant as possible, the optimization algorithm recognizes that the best trajectory is the one who follows the free dynamic for as long time as possible, i.e. almost for one orbital period. Then the spiral decreases and collapse towards the target by means of control's application.

The code prepared for the present study starts from the computation of the desired optimal trajectory, which is used as a reference for the closed loop control evaluation. A GNC loop is implemented to simulate real time behaviour of the Navigation and Control structures. An Unscented H-Infinity filter is used for the relative state estimation. This filter was selected with respect to more typical solutions because it deals better with complex measures equations, as its being an Unscented filter, and because it is a robust conservative filter as it minimizes the worst case error, while Kalman filters are minimum covariance-based filters. More results regarding comparison between H-infinity and Kalman filters can be found in [6], while H-infinity's mathematical derivation and structure is presented in [7], [8] and [9]. A test case maneuver has to be chosen in order to study the impact of target's illumination and observation conditions on the maneuver's success.

First of all, the target is supposed to orbit on a midday-midnight sun synchronous orbit with the following orbital parameters

$$
\begin{aligned}
a &= 7500\,km \\
e &= 0.1 \\
i &= 99.87° \\
\Omega &= 150° \\
\omega &= 100° \\
\nu_0 &= 0°
\end{aligned}
\tag{1}
$$

This choice has been driven from the need to have some eclipse periods, where the camera doesn't give any output, in order to test the robusteness of the GNC structure to every kind of contingencies. The target's orbit is presented in Figure 1, where the earth-to-sun vector at maneuver's first instant is also plotted. The earth's ephemeris, expressed in the ECLIPJ2000 reference frame, are taken from the Spice kernels [10].
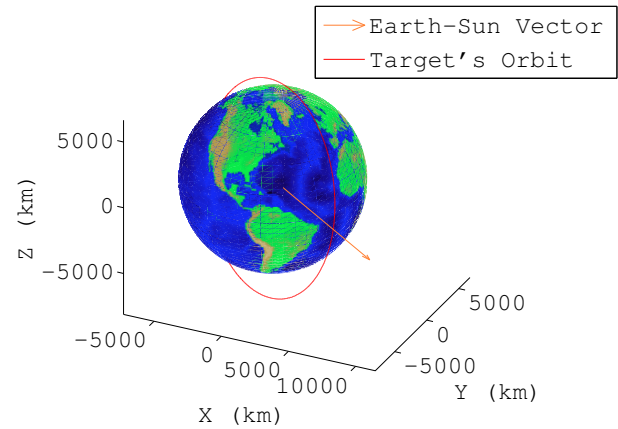

Figure 1. **Target's orbit and earth-to-sun vector at maneuver's first instant.**

The initial relative conditions, expressed in the Local Vertical - Local Horizontal or HILL reference frame[2], are chosen to be the following

$$
\begin{aligned}
x_0 &= 100\,m \\
y_0 &= 100\,m \\
z_0 &= 200\,m \\
\dot{x}_0 &= 0.1\,m/s \\
\dot{y}_0 &= 1\,m/s \\
\dot{z}_0 &= 0\,m/s
\end{aligned}
\tag{2}
$$

We consider here a fixed and known shape for the target, which is shown in Figure 2, where the docking point is identified in the target's body frame.

---

[2]In the Local Vertical - Local Horizontal or HILL reference frame the origin is in the target's centre of mass, $\hat{\mathbf{x}}$ axis is parallel to target' position vector $\mathbf{r_0}$, $\hat{\mathbf{y}}$ axis is the in-plane normal to the radius vector $\mathbf{r_0}$ and $\hat{\mathbf{z}}$ axis is parallel to target's orbit's angular momentum.
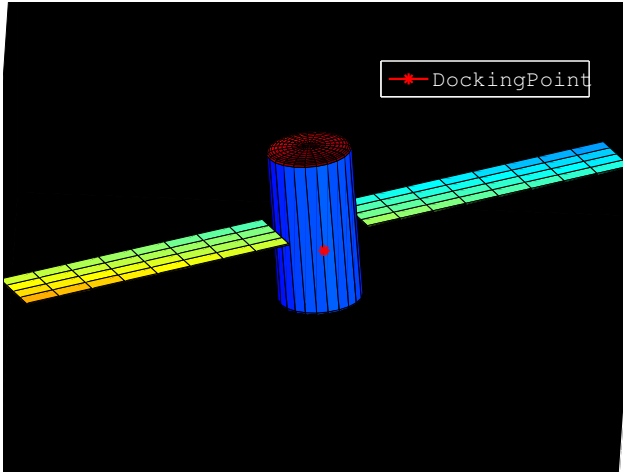
2

Figure 2. **Target's shape and Docking Point.**

Two test cases are presented with the same orbital parameters and initial conditions:

1. the target is considered to be constantly nadir pointing towards the earth

$$\boldsymbol{\omega}_1 = (0,\, 0,\, n)^T$$
$$n = \sqrt{\mu_\oplus/a^3} = 9.72 \times 10^{-4}\ rad/s \tag{3}$$

2. the target tumbles freely with a chosen fixed spinning velocity

$$\boldsymbol{\omega}_t = (0.1,\, 0,\, 0.1)^T\ \ rad/s \tag{4}$$

The final conditions are obtained by propagating the target's attitude by means of the Euler equations for the time of the maneuver which, as previously discussed, can be conveniently set as $t_m = 0.9T = 6300\,s$. Knowing the target's attitude at the final time t_f and the coordinates of the docking point with respect to the target's body frame, it is thus possible to compute the final relative conditions.

Given the initial and final constraints and the target's orbit, we use the optimization algorithm presented in [6] to compute the optimal docking trajectory, which will be used as a reference trajectory to which we want our estimated state to converge. As the target's spinning velocities are different in the two cases presented above, we obtain two different maneuvers, which are plotted in Figure 3 and 4.

We recall that the dynamic equations used are the well-known Tschauner-Hempel equations[11], which have been modified to take into account the drag perturbation acting on both the target and the chaser (see [6])

$$\ddot{x} = 2\omega_0 \dot{y} + \dot{\omega}_0 y + \omega_0^2 x - \frac{\mu}{||\mathbf{r_0} + \boldsymbol{\rho}||^3}(r_0 + x) +$$
$$+ \frac{\mu}{r_0^2} + D_{1,x} - D_{0,x} \tag{5a}$$

$$\ddot{y} = -2\omega_0 \dot{x} - \dot{\omega}_0 x + \omega_0^2 y - \frac{\mu}{||\mathbf{r_0} + \boldsymbol{\rho}||^3}y +$$
$$+ D_{1,y} - D_{0,y} \tag{5b}$$

$$\ddot{z} = -\frac{\mu}{||\mathbf{r_0} + \boldsymbol{\rho}||^3}z + D_{1,z} - D_{0,z} \tag{5c}$$

where $\mathbf{D}$ is the drag perturbation acting on the spacecraft and the subscripts 0 and 1 refer respectively to target and chaser.

The open loop Δv needed to follow the optimum trajectories are, for the two cases:

$$\Delta v_1 = 2\,m/s \tag{6}$$
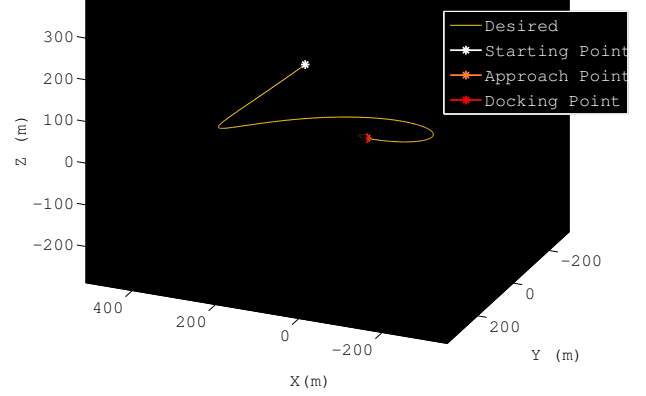$$\Delta v_2 = 2.52\,m/s \tag{7}$$

Figure 3. **Case 1, nadir pointing. Plot of the Desired relative trajectory, expressed in the Hill reference frame.**
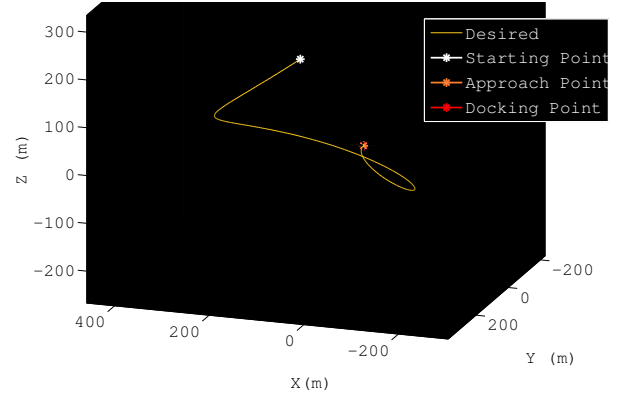

Figure 4. **Case 2, free tumbling. Plot of the Desired relative trajectory, expressed in the Hill reference frame.**

3. INSTRUMENTS' NOISE

Angles of visibility

In order to evaluate the performance of the sensors, some parameters which affect the measurement noise have to be found. According to [12], the accuracy of the measurements given by a LIDAR depends on the angle with which the instrument is observing the body, i.e. the *Sight Angle* γ between the LIDAR's line of sight and the normal to the observed body's surface.

The law describing the dependence between the measure's noise and the sight angle is shown in Figure 5. The red curve is plotted by fitting the experimental results obtained

3

by taking measures with different incidence angles and can be analytically expressed through a nine-degree polynomial such as

$$\sigma_\rho = \sum_{i=0}^{9} a_i \gamma^i \tag{8}$$

where the a_i coefficients are computed by superimposing the constraints identified as the red points in Figure 5.
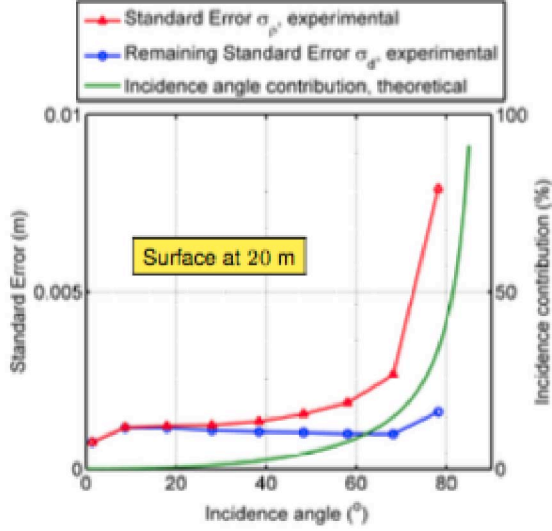

Figure 5. **Measurement accuracy as function of the surface's incidence angle, given a fixed source distance (from [12]).**

We notice that the noise graph presented above is valid for measurements taken at 20 meters. For measurements taken at different distances, we assume that the law described scales linearly with the distance, that is

$$\sigma_\rho(x) = \frac{\sigma_\rho(x = 20)}{20} x \tag{9}$$

Similarly, covariance variations in the camera's measurements can be found depending on the target's illumination conditions. When the target is not in eclipse, images can be taken and azimuth and elevation angles can be computed by tracking features through several images. However, the information which can be extracted by an image depends on the light intensity with which the target is illuminated.

This aspect can be taken into account by defining two angles, which are shown in Figure 6:

• *Illumination Angle θ*: the angle of the sun's incidence on the target;
• *Resolution Angle ψ*: the angle between the sun ray illuminating the target and the camera's line of sight.

We assume that the law which describes the degradation of the camera's measurements noise is given, for both azimuth and elevation, by
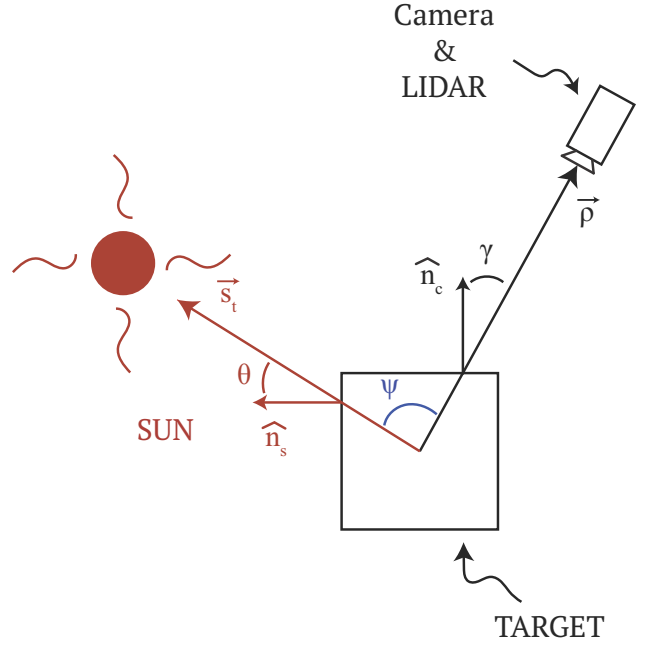
$$\sigma = \frac{\sigma_0}{\cos\theta \cos\psi} \tag{10}$$

Figure 6. **Visibility angles. In red: the angle θ between the sun ray and the target's normal. In black: the angle γ between the LIDAR's line of sight and the target's normal. In blue: the angle ψ between the camera line of sight and the sun ray.**

where σ_0 is the covariance in the best configuration, i.e. when the camera line of sight and the solar rays are parallel and normal to the target surface. This number can be set as $10^{-3}\, rad$ for both angles, as done in [13].

We can compute the three visibility angles as follows

$$\gamma = \arccos\left(\frac{\boldsymbol{\rho} \cdot \hat{\mathbf{n}}_c}{\|\boldsymbol{\rho} \cdot \hat{\mathbf{n}}_c\|} \right) \tag{11}$$

$$\theta = \arccos\left(\frac{\mathbf{S_t} \cdot \hat{\mathbf{n}}_s}{\|\mathbf{S_t} \cdot \hat{\mathbf{n}}_s\|} \right) \tag{12}$$

$$\psi = \arccos\left(\frac{\mathbf{S_t} \cdot \boldsymbol{\rho}}{\|\mathbf{S_t} \cdot \boldsymbol{\rho}\|} \right) \tag{13}$$

We notice that the first two angles can't be larger than 90 degrees, while the resolution angle can assume values between 0 and 180 degrees. A resolution angle larger than 90 degrees doesn't mean that no measures can be taken, but if used in (10) will give a negative covariance, which has no physical meaning. Indeed, the degradation will be set to its maximum (attained for $\psi = 90°$) for any $\psi >= 90°$.

As these three angles depend on the $\boldsymbol{\rho}$ vector, it follows that their profile in time changes if we consider different docking paths. In turn, changing the approach trajectory affects the visibility angles' profiles and thus the accuracy of the measures received and used to estimate the system's state. As the estimation of the state is used in the closed loop control law, which determines the real amount of Δv used for the maneuver, it follows that the degradations on the measures influence the maneuver performance. Indeed, the optimal design of the trajectory shall take into account measurements' degradation.

4

Considering the two test cases reported in Section 2, we can use the desired trajectory to compute the visibility angles profiles and have a preliminary idea of their impact on the future trajectory estimation process. The resulting angles' time histories are plotted in Figure 7 and 8 for the two test cases. The profiles are smoother and more regular in case 1 than in case 2 because the target's spin velocity is much lower in the first case and the nadir pointing configuration on a sun synchronous orbit is such that the illumination conditions are periodic. Notice that eclipse computation has not been included here yet.

According to the hypothesis represented by equation (10), it is reasonable to think that these variations will change the measures' covariances in a way that will strongly degrade the maneuver's performance.
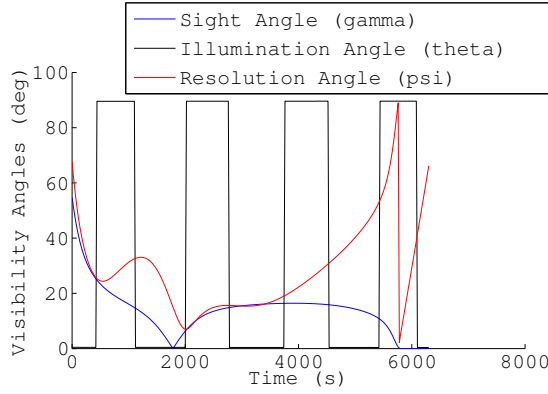

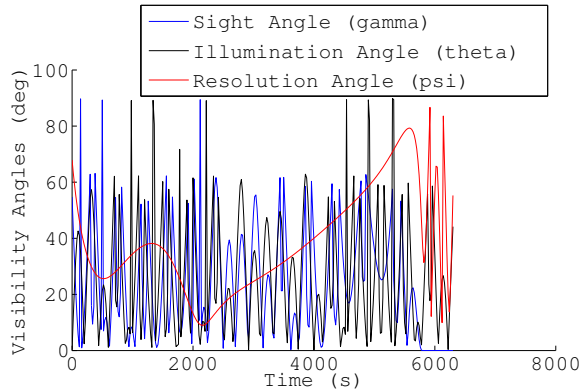**Figure 7**. **Case 1, nadir pointing. Plot of the visibility angles profiles throughout the maneuver.**

Figure 8. **Case 2, free tumbling. Plot of the visibility angles profiles throughout the maneuver.**

4. RESULTS

As a first step for showing the impact of the measures' degradation of the maneuver's performance we present the results obtained with constant noise throughout the trajectory (see also [6]). Please note that, from now on, we will present Δv obtained as typical values provided by the minimum propellant consumption optimal solver (see Section 2).

The covariances used are $\sigma_\rho = 1e-6\,km$ for the LIDAR and $\sigma_{el} = \sigma_{az} = 1e-3\,rad$ for the camera [13]. We use the the trajectories presented in Section 2 and plotted in Figure 3 and

4 as the reference to converge at. The control used is a closed loop control constant over the k-th time interval

$$\mathbf{u_k} = -\mathbf{K_k}\left(\hat{\mathbf{x}}_\mathbf{k} - \mathbf{x_{d,k}}\right) \qquad (14)$$

where:

- the gain matrix K_k is computed by means of the well-known Linear Quadratic Regulator method, where R and Q mare respectively a 3×3 and a 6×6 diagonal matrices. The chosen weights are: $q_1 = 10^2$ for position's components, $q_2 = 10^2$ for velocity's components and $r_x = r_y = r_z = 10^{10}$ for control's components. Notice that the gain matrix has to be evaluated at each instant because the dynamic matrix A depends on the target's orbital angular velocity (which varies with the time as the target is on an elliptical orbit);
- $\hat{\mathbf{x}}_k$ is the estimated state at t_k;
- $\mathbf{x_{d,k}}$ is the desired state at t_k.

The estimated state $\hat{\mathbf{x}}_k$ is evaluated at each instant by means of an Unscented H-Infinity Filter. According to [8] and [9], the constants needed by the filter as set as $\alpha = 10^{-1}$, $\beta = 2$ and $\xi = 30$. The state is considered known at the beginning of the maneuver with an error equal to $\varepsilon = 10^{-2}\,km$ for the position components and $\varepsilon = 5 \times 10^{-4}\,km/s$ for the velocity components.

The maneuver time, the closed loop Δv and the maximum covariance on the state components are parameters typically helpful to evaluate the performance of such a class of maneuvers. In this case we fix the maneuver time to a certain value, so only the latter two will be used.

The closed loop Δv needed for the maneuver is $\Delta v_{cl,1} = 4.28\,m/s$ for the nadir pointing case and $\Delta v_{cl,2} = 6.44\,m/s$ for the second case. The covariances on the state components, captured at the 10-th iteration when the filter had already started to converge, are presented in Table 1 for the two cases.

Table 1. **Nominal cases. Covariances at 10-th iteration.**

	Nadir Pointing	**Free Tumbling**
σ_x (km)	2.39×10^{-4}	2.40×10^{-4}
σ_y (km)	1.97×10^{-4}	1.96×10^{-4}
σ_z (km)	2.71×10^{-4}	2.69×10^{-4}
$\sigma_{\dot{x}}$ (km/s)	4.3×10^{-6}	4.36×10^{-6}
$\sigma_{\dot{y}}$ (km/s)	3.46×10^{-6}	3.42×10^{-6}
$\sigma_{\dot{z}}$ (km/s)	4.78×10^{-6}	4.78×10^{-6}

From now on we will refer to the presented results as the nominal cases as they set the best-case scenario to which we will compare the results obtained by using the measures' noise models presented in Section 3.

Degraded measures

First of all, we compare the nominal cases, which are obtained with the smallest possible covariance, with two cases where the covariances follow the laws (9) and (10). We assume here that both the measures from the LIDAR and the camera are available at each instant. This means we are not considering any eclipse at the moment. Moreover, if any of the visibility angles is greater than a certain chosen threshold

5

value, that we set to 85 degrees, we will assume that we get a measure with that angle equal to the threshold value.

In Figure 9 we can see the output of the GNC algorithm, where the desired, true and estimated trajectories are plotted, while in Figure 10 the differences between desired and true position and estimated and true position for the entire maneuver length are shown. In Figure 11 and 12 the LIDAR's and camera's covariances are plotted. The plots for the free tumbling case are presented in Figure 13, 14, 15 and 16.

As we can see in Figure 11 and 12, the covariances are always greater than the minimum values used for the nominal cases and, in some intervals, the camera covariance are even two orders of magnitude larger than the minimum one.

Despite the large difference in covariance, the performance still remains quite similar to the nominal case. This can be seen in Table 2 where the covariances obtained by the Unscented H Infinity Filter at iteration number 10 are listed for the two cases. Moreover, the Δv obtained in these two cases are respectively $\Delta v_{d,1} = 4.33\,m/s$ and $\Delta v_{d,2} = 4.65\,m/s$.

As the results obtained for the two degraded case don't differ significantly to the nominal cases' results, we can affirm that the maneuver is feasible under measurements' degradation assumption.

Table 2. **Degraded measures cases. Covariances at 10-th iteration.**

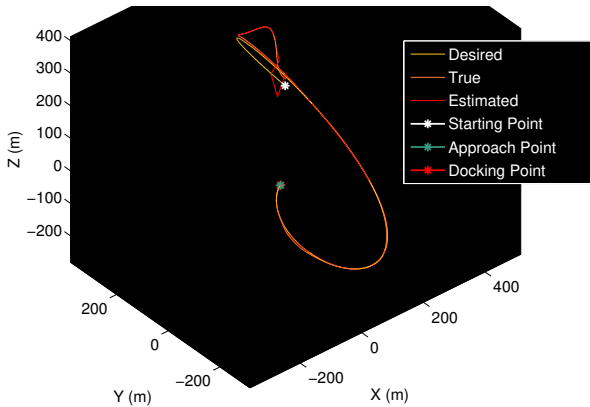|	**Nadir Pointing**	**Free Tumbling**
σ_x (km)	3.20×10^{-4}	3.41×10^{-4}
σ_y (km)	2.70×10^{-4}	2.85×10^{-4}
σ_z (km)	3.58×10^{-4}	3.84×10^{-4}
$\sigma_{\dot{x}}$ (km/s)	5.67×10^{-6}	6.36×10^{-6}
$\sigma_{\dot{y}}$ (km/s)	4.96×10^{-6}	5.27×10^{-6}
$\sigma_{\dot{z}}$ (km/s)	6.23×10^{-6}	6.90×10^{-6}

Figure 9. **Case 1, nadir pointing. Plot of the desired, true and estimated relative trajectory, expressed in the Hill reference frame, for the degraded measurements scenario.**
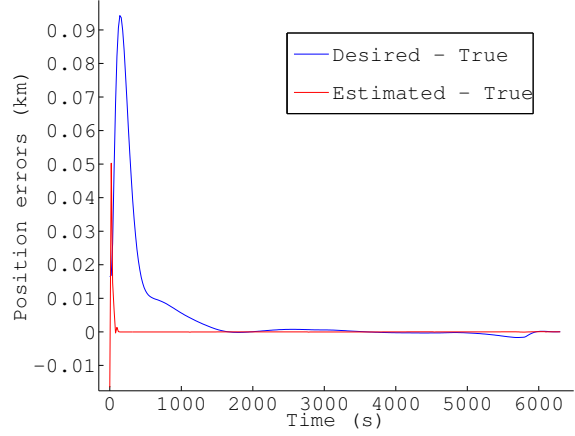

Figure 10. **Case 1, nadir pointing. Plot of the differences (errors) between desired and true position (blue) and estimated and true position (red), for the degraded measurements scenario.**
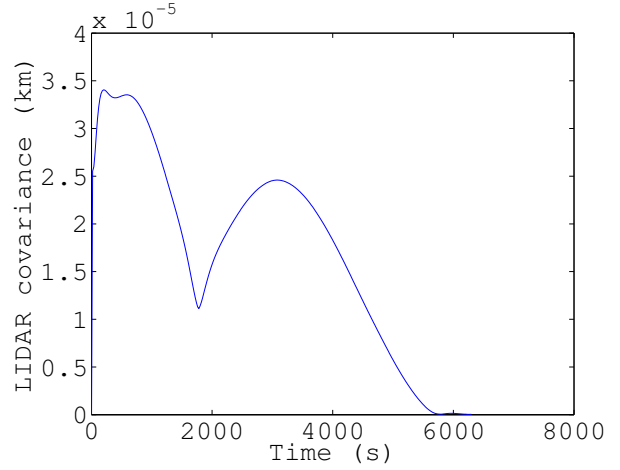

Figure 11. **Case 1, nadir pointing. Plot of the LIDAR covariance profile throughout the maneuver for the degraded measurements scenario.**

Eclipse case

Going one step further, to get closer to reality, we are going to consider the target eclipses throughout the maneuver. When the target is in eclipse the camera can no longer collect images of the target. Therefore, the only measure available to the chaser is the range obtained from the LIDAR.

Moreover, we assume that the portion of measures obtained by LIDAR and camera when the angles are greater than the threshold value, set to 85 degrees, are not usable for the estimation process. Different possibilities can occur:

• if the sight angle γ is greater than the threshold value no measure will be taken from the LIDAR;
• if either the illumination θ or the resolution angle ψ are greater than the threshold value no measure will be taken from the camera;
• if both the conditions above happen, no measures will be taken at all.
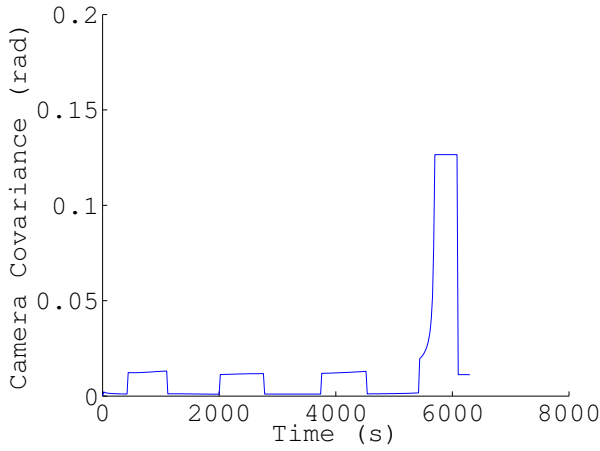
6

Figure 12. **Case 1, nadir pointing. Plot of the camera covariance profile throughout the maneuver for the degraded measurements scenario.**
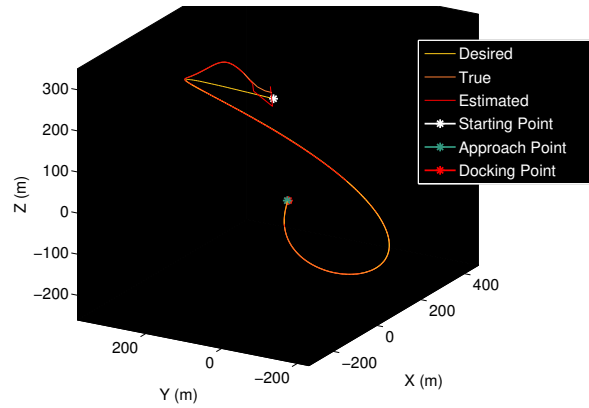

Figure 13. **Case 2, free tumbling. Plot of the desired, true and estimated relative trajectory, expressed in the Hill reference frame, for the degraded measurements scenario.**
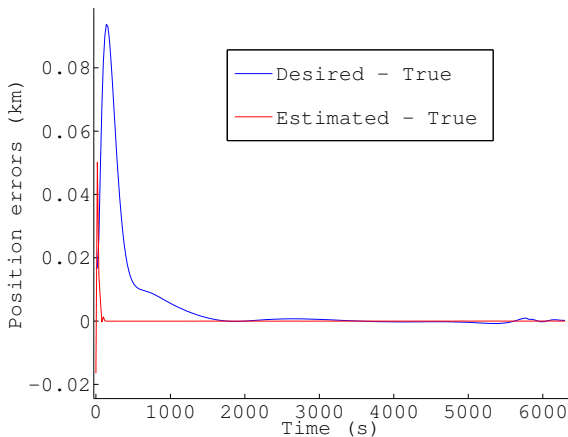

Figure 14. **Case 2, free tumbling. Plot of the differences (errors) between desired and true position (blue) and estimated and true position (red), for the degraded measurements scenario.**
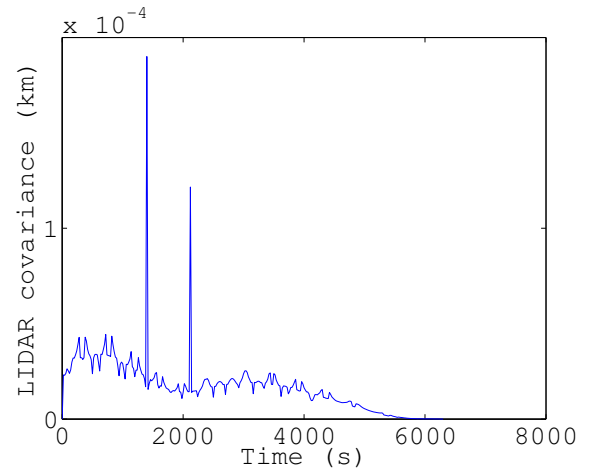

Figure 15. **Case 2, free tumbling. Plot of the LIDAR covariance profile throughout the maneuver for the degraded measurements scenario.**
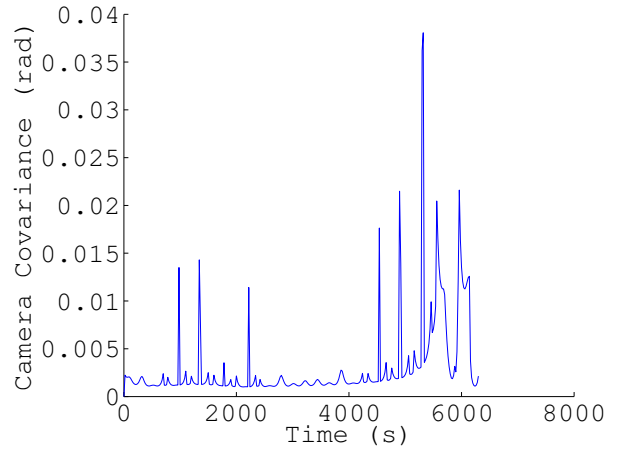

Figure 16. **Case 2, free tumbling. Plot of the camera covariance profile throughout the maneuver for the degraded measurements scenario.**

In the last case the estimate of the state at t_{k+1} will be obtained by propagating the state at t_k through the dynamic equations.

In Figure 17 and 18 the portion of trajectory where the target is in eclipse is showed, i.e. the portion of trajectory where no camera measurements will be taken.

In Figure 19 the output of the GNC algorithm for the nadir point case is plotted, while in Figure 20 the differences between desired and true position and estimated and true position for the entire maneuver length are shown. In Figure 21 and 22 the covariances profiles are plotted. For the latter, we plotted a covariance value equal to zero when no measures are taken. The same graphs are shown in Figure 23, 24, 25 and 26 for the free tumbling case.

By giving a close and careful look at Figure 21, 22, 25 and 26, we can see that the measures are taken in the first steps of the maneuver, precisely till $\bar{t} = 420\,s$, for both the nadir pointing and the free tumbling scenarios. As no parameter has been changed between the degraded test-cases and the last
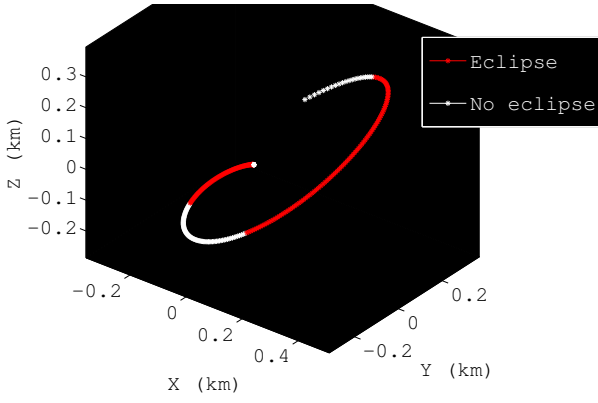
7

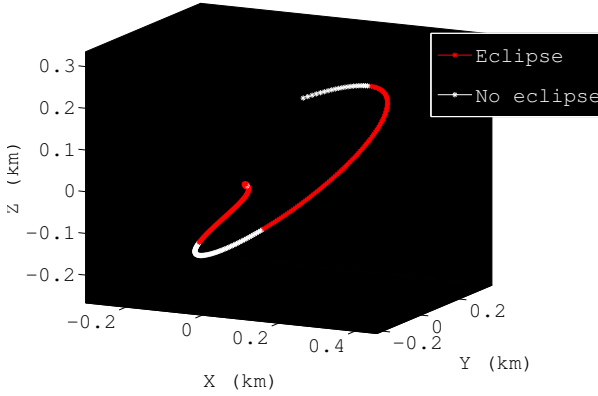**Figure 17**. **Case 1, nadir pointing. Plot of the eclipse intervals during the approach maneuver.**

Figure 18. **Case 2, free tumbling. Plot of the eclipse intervals during the approach maneuver.**
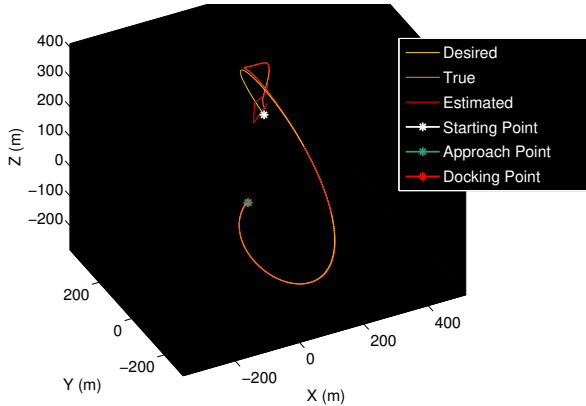

Figure 19. **Case 1, nadir pointing. Plot of the desired, true and estimated relative trajectory, expressed in the Hill reference frame, obtained with the inclusion the target's eclipses.**

Figure 20. **Case 1, nadir pointing. Plot of the differences (errors) between desired and true position (blue) and estimated and true position (red), obtained with the inclusion of the target's eclipses.**

Figure 21. **Case 1, nadir pointing. Plot of the LIDAR covariance profile throughout the maneuver obtained with the inclusion the target's eclipses.**

ones, and considering that the 10-th iteration corresponds to $t^* = 200\,s$ as the step between the measurements acquisition is $\Delta t = 20\,s$, no large differences between the covariances of the degraded cases, listed in Table 2, and the covariances obtained in the last two scenarios are expected. Simulations' findings confirm this analysis.
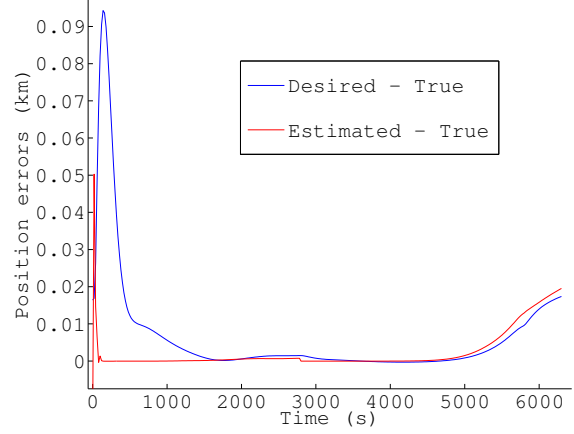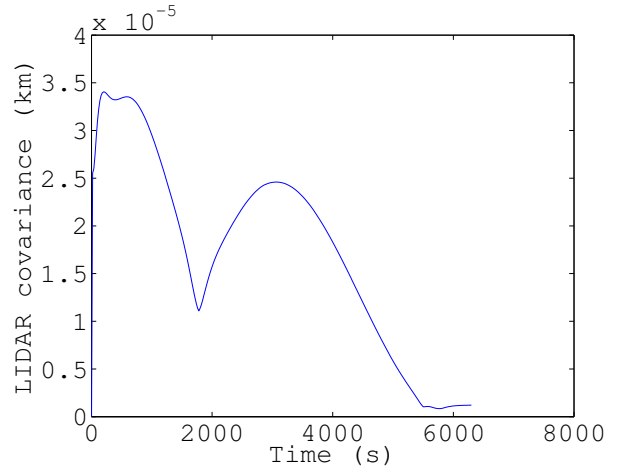
Because the eclipses are situated ahead in the maneuver, and because no measurements are taken for a long period roughly from $4000\,s$ on (as we can see in Figure 22 and 26), it is reasonable to think that differences will be noted if some parameters regarding the last part of the maneuvers are analyzed.

Precisely, we will focus on the position and velocity errors at the end of the maneuver and on their mean throughout the maneuver. We first define two class of errors in this problem:

- the *desired error* ε_d, which is the difference between the true position/velocity and the desired position velocity;
- the *estimation error* ε_e, which is the difference between the estimated position/velocity and the true position/velocity.

Thus, we have four final errors for each case $\varepsilon_{d,\rho}^f$, $\varepsilon_{d,\dot\rho}^f$, $\varepsilon_{e,\rho}^f$ and $\varepsilon_{e,\dot\rho}^f$, respectively: final desired error in position and velocity, final estimation error in position and velocity.
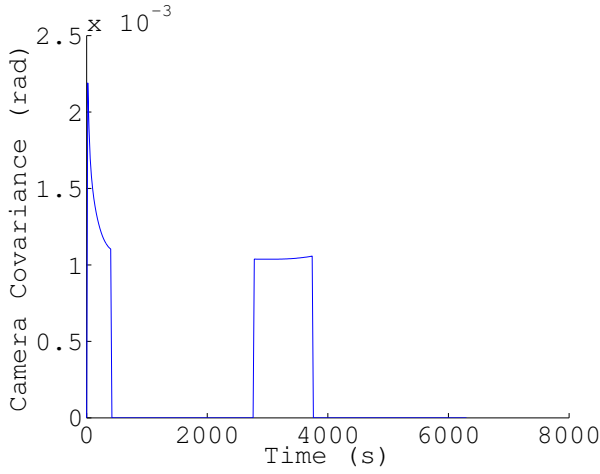
8

Figure 22. **Case 1, nadir pointing. Plot of the camera covariance profile throughout the maneuver obtained with the inclusion the target's eclipses.**
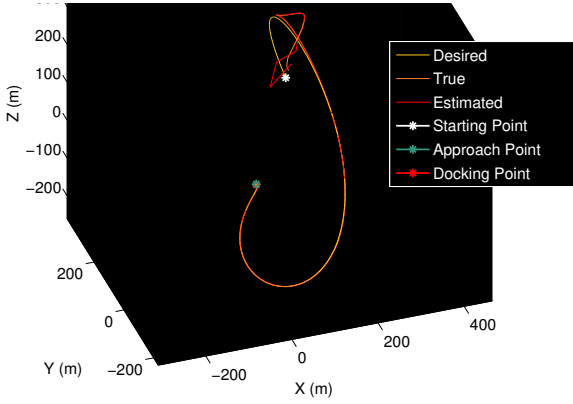

Figure 23. **Case 2, free tumbling. Plot of the desired, true and estimated relative trajectory, expressed in the Hill reference frame, obtained with the inclusion the target's eclipses.**
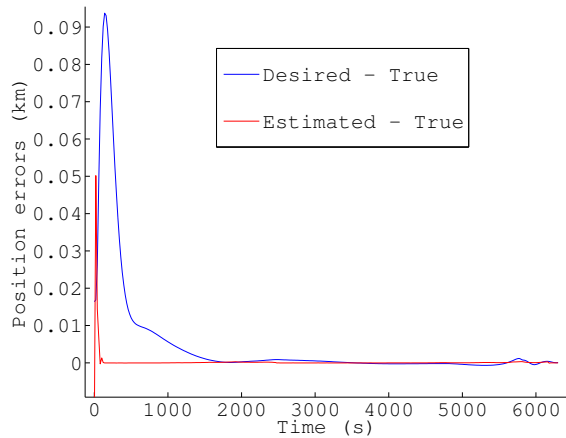

Figure 24. **Case 2, free tumbling. Plot of the differences (errors) between desired and true position (blue) and estimated and true position (red), obtained with the inclusion of the target's eclipses.**
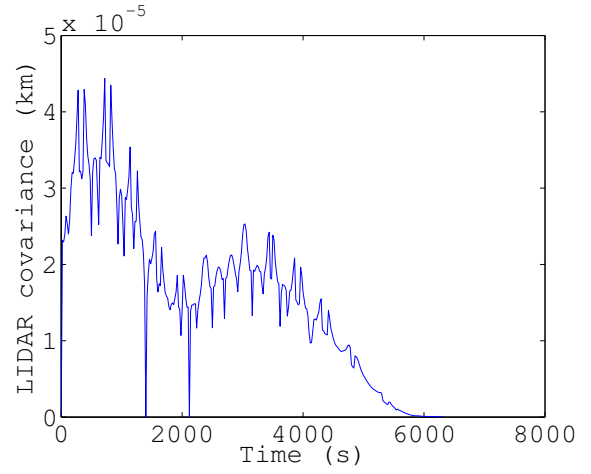

Figure 25. **Case 2, free tumbling. Plot of the LIDAR covariance profile throughout the maneuver obtained with the inclusion the target's eclipses.**
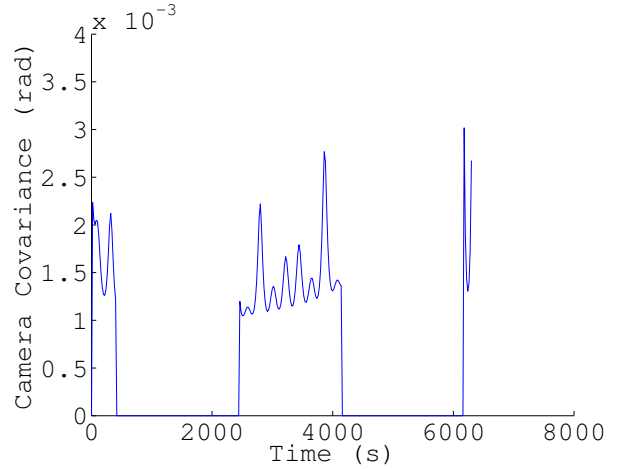

Figure 26. **Case 2, free tumbling. Plot of the camera covariance profile throughout the maneuver obtained with the inclusion the target's eclipses.**

We also consider the mean position error throughout the entire maneuver, obtained as follows

$$\bar{\varepsilon}_\rho = \frac{\sum_{i=1}^{N} \varepsilon_{d,\rho}^i + \varepsilon_{e,\rho}^i}{N} \qquad (15)$$

The errors are listed in Table 3 where the nadir pointing scenario with degraded measures and with eclipse are compared. As we can see in Table 3, the final and mean errors are greater in the eclipse case than in the degraded measures case. This happens because, even though the camera's covariances are quite high and so the result in the degraded measure scenario is strongly affected by low accuracy measurements, in the eclipse case there are large periods where no measure is taken from the camera at all, i.e. roughly from $420\,s$ and $2700\,s$ and from $3800\,s$ till the end of the maneuver (see Figure 22). In these time intervals the only information acquired is the range measure given by the LIDAR, which instead is always available, as can be seen in Figure 21. However, this single information, along with dynamic propagation, is not sufficient to give better results than in the degraded measures scenario.

9

The final errors are high if compared to the scale of the problem, in fact the position error is of the same order as the initial position. Although a better result is achieved with velocities, we can conclude that the maneuver is not feasible in this nadir pointing configuration if only range measures are available during target's eclipses.

Table 3. Case 1, nadir pointing. Comparison of final and mean errors between degraded measures and eclipse scenarios.

	Degraded measures	Eclipse
$\varepsilon_{d,\rho}^f$ (km)	5.46×10^{-5}	1.67×10^{-2}
$\varepsilon_{d,\dot{\rho}}^f$ (km/s)	2.77×10^{-6}	1.42×10^{-5}
$\varepsilon_{e,\rho}^f$ (km)	1.27×10^{-6}	1.89×10^{-2}
$\varepsilon_{e,\dot{\rho}}^f$ (km/s)	-1.14×10^{-8}	-4.45×10^{-6}
$\bar{\varepsilon}_\rho$ (km)	4.95×10^{-3}	9.19×10^{-3}

In Table 4 the errors for the free tumbling scenario are listed. The degraded measures and eclipse cases are compared by means of the final and mean errors.

Differently from the nadir pointing scenario, we have that the final errors are lower in the eclipse case than in the degraded measures one. This can initially seem wrong, but the explanation to this phenomena can be found in the camera's covariances.

By giving a look at Figure 16 we can see how big the camera covariance averagely is in the degraded measures scenario. It touches maximum values of $4 \times 10^{-2} \, rad$ and the mean value increases in the last intervals of the maneuver.

If we now switch our focus on Figure 26, we easily see how the camera covariance in the eclipse scenario is averagely much lower than the degraded measure scenario. The maximum value is roughly $3 \times 10^{-3} \, rad$, while there is no increase in the last part of the maneuver, since no measures are taken at all in that phase. On the other hand, there are time intervals when the camera measures can't be taken, either because of high visibility angles' values or because the target is in eclipse.

The comparison between these two scenarios is based on a trade-off between two aspects:

1. having more measures with lower accuracy;
2. having less measures with higher accuracy.

In this case, the second aspect is prevailing. Moreover, as we considered the final errors as comparison parameters, it is worse to have low-accuracy measurements at the final phase of the maneuver (as in Figure 16) rather than not having them at all (as in Figure 26) and letting the filter work only with LIDAR's measures. In fact, if we consider the mean position error throughout the entire maneuver, we can see how it is bigger in the eclipse scenario, which confirms the theory that is averagely better to have more measures, even if with low accuracies.

Hypothetically, it is reasonable to affirm that, under different target's orbit scenarios, worse results would be possible for the eclipse case. This could for example happen if the eclipse interval was situated during the first phase of the maneuver. This because the filter needs to converge in the first steps and

Table 4. Case 2, free tumbling. Comparison of final and mean errors between degraded measures and eclipse scenarios.

	Degraded measures	Eclipse
$\varepsilon_{d,\rho}^f$ (km)	2.06×10^{-4}	5.23×10^{-5}
$\varepsilon_{d,\dot{\rho}}^f$ (km/s)	4.30×10^{-6}	3.60×10^{-6}
$\varepsilon_{e,\rho}^f$ (km)	2.11×10^{-7}	-1.68×10^{-6}
$\varepsilon_{e,\dot{\rho}}^f$ (km/s)	-1.09×10^{-7}	-9.94×10^{-8}
$\bar{\varepsilon}_\rho$ (km)	4.99×10^{-3}	5.10×10^{-3}

the process would be much more difficult with no measures available.

On the other hand, it is at the same time reasonable to think that, if no eclipse was present during the very last steps of the maneuver, which are the most delicate one, results in the nadir pointing scenarios would change, and the maneuver would be feasible.

Moreover, the feasibility of the maneuver is strongly influenced by the visibility angles, which determine whether any measure is available or not. As they depend on both the chaser relative position, target's spin velocity and target's orbit, we can assume that they can have a different impact for every possible case.

As a conclusion, we can say that there is the possibility to create a *Feasibility Chart*, where for each possible configuration of initial and final conditions, target's orbit and target's spin velocity the feasibility of the maneuver is assessed.

This brings to the need to give the word *feasibility* a proper definition, which can for example be: "A maneuver is feasible when the docking is successful". This condition can in turn be translated into a low level requirement such as: "The final position and velocity errors have to be lower than a user-defined threshold value".

Infrared measures

In order to be sure that the system is fulfilling the task as desired, we can make our system even more robust by installing on-board an infrared sensor (as suggested in [14]), which provides the navigation algorithm with thermal measures when the target is in eclipse and no observation can be made in the visible spectra.

According to the standard performance of infrared systems, that lag with respect to visible hardware, we can assume for this device

$$\sigma_{ir} = 2 \times 10^{-2} \, rad \qquad (16)$$

i,.e. a conservative value 20 times larger than the one of the visible camera.

We now want to see how the GNC behaviour is modified by considering thermal measures to be available during target's eclipses.

In Figure 27 the covariances of both the camera and the infrared sensor are plotted. The profile is the same as the one in Figure 22 with the difference that when the target is in eclipse we use the infrared sensor, thus having a covariance equal to $2 \times 10^{-2} \, rad$, which is the maximum value in Figure 27. The intervals where the covariance is still zero are the

time intervals when the target is not in eclipse, but either the illumination angle or the resolution angle are greater than the threshold value, which means that no measure is available from the camera and can not be replaced by an infrared measure.
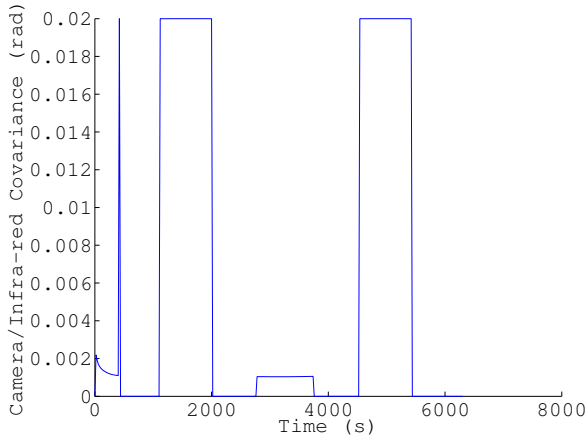

Figure 27. **Case 1, nadir pointing. Camera and infrared covariances throughout the maneuver.**

In Table 5 the final and mean errors are listed for the cases with and without the infrared sensor available, for the nadir pointing scenario.

We can see that the final errors are lower if we have the possibility to take infrared measures while the target is in eclipse, even though those measures have a low accuracy. This happens because, as explained in Section 4, the eclipse periods are long at the point that even a low accuracy measure is a better information than no measure at all.

Table 5. **Case 1, nadir pointing. Comparison of final and mean errors between infrared and eclipse scenarios.**

	Infrared sensor	No infrared sensor
$\varepsilon^f_{d,\rho}$ (km)	1.35×10^{-3}	1.67×10^{-2}
$\varepsilon^f_{d,\dot\rho}$ (km/s)	6.78×10^{-7}	1.42×10^{-5}
$\varepsilon^f_{e,\rho}$ (km)	1.64×10^{-3}	1.89×10^{-2}
$\varepsilon^f_{e,\dot\rho}$ (km/s)	-1.64×10^{-6}	-4.45×10^{-6}
$\bar\varepsilon_\rho$ (km)	5.29×10^{-3}	9.19×10^{-3}

The opposite effect is obtained for the free tumbling scenario, where we have already seen that it is better to have less measures with higher accuracy rather than having a lot of measures with low accuracy.

5. SUMMARY

The impact of illumination conditions on the performance of a specific test-case maneuver has been studied. The state covariances at the 10-th iteration, the maneuver Δv, the final and mean errors in position and velocity have been chosen as significant performance evaluation parameters. These parameters depend in fact on the navigation output, i.e. the state estimation, which in turn depends on the measures' covariances.

It has shown how the measures' noises strongly depend on the measuring distance and the sight angle for the LIDAR [12]. On the other hand, we assumed a certain model for the dependence between the camera covariance and the visibility angles. It has been moreover shown that the presence or absence of target's eclipse periods influences the performance evaluation parameters.

It has been proved that the feasibility of the test case maneuver can be confirmed for the nadir pointing case, while it is denied for the free tumbling target in presence of long eclipse periods due to the particular configuration chosen.

In addition, the presence of an infrared sensor on-board has been assumed in the very last step of this speculation in order to verify if the presence of degraded measures during target's eclipse periods would have increased the chance of mission success.

The parameters influencing the feasibility of the maneuver, i.e. the initial and final condition, the target's orbit, spin velocity, shape and initial attitude, can be varied in a hyper-volume containing all possible scenarios to assess the feasibility of the maneuver and verify if there are sub-volumes contained in the entire volume in which the maneuver is considered as feasible to certain requirements. We recall the possibility to carry out such a research and develop new GNC code's blocks and algorithms, along with new instrumentation configurations which would provide the system with more robusteness and would increase the number of test-cases for which the feasibility of the maneuver is confirmed.

REFERENCES

[1] R. T. Howard, T. C. Bryan, M. L. Book, and R. W. Dabney, "The video guidance sensor-a flight proven technology," 1999.

[2] A. C. Allen, C. Langley, R. Mukherji, A. B. Taylor, M. Umasuthan, and T. D. Barfoot, "Rendezvous lidar sensor system for terminal rendezvous, capture, and berthing to the international space station," in *SPIE Defense and Security Symposium*. International Society for Optics and Photonics, 2008, pp. 69 580S–69 580S.

[3] D.-M. Cho, D. Jung, and P. Tsiotras, "A 5-dof experimental platform for autonomous spacecraft rendezvous and docking," *AIAA Paper*, vol. 1869, p. 2009, 2009.

[4] P. Gasbarri, M. Sabatini, and G. Palmerini, "Ground tests for vision based determination and control of formation flying spacecraft trajectories," *Acta Astronautica*, vol. 102, pp. 378–391, 2014.

[5] P. Jasiobedzki, S. Se, T. Pan, M. Umasuthan, and M. Greenspan, "Autonomous satellite rendezvous and docking using lidar and model based vision," in *Defense and Security*. International Society for Optics and Photonics, 2005, pp. 54–65.

[6] R. Volpe, "Choreography on elliptical orbit," Master's thesis, University of Rome "La Sapienza", 2016.

[7] W. Li and Y. Jia, "H-infinity filtering for a class of non-linear discrete-time systems based on unscented transform," *Signal Processing*, vol. 90, no. 12, pp. 3301–3307, 2010.

11

[8] S. J. Julier, J. K. Uhlmann, and H. F. Durrant-Whyte, "A new approach for filtering nonlinear systems," in *American Control Conference, Proceedings of the 1995*, vol. 3. IEEE, 1995, pp. 1628–1632.

[9] D. Simon, *Optimal state estimation: Kalman, H infinity, and nonlinear approaches*. John Wiley & Sons, 2006.

[10] https://naif.jpl.nasa.gov/naif/data.html.

[11] H. Schaub and J. L. Junkins, *Analytical mechanics of space systems*. Aiaa, 2003.

[12] S. Soudarissanane, R. Lindenbergh, M. Menenti, and P. Teunissen, "Incidence angle influence on the quality of terrestrial laser scanning points," in *Proceedings IS-PRS Workshop Laserscanning, Paris, France*. ISPRS, 2009.

[13] M. Vetrisano and M. Vasile, "Autonomous navigation of a spacecraft formation in the proximity of an asteroid," *Advances in Space Research*, vol. 57, no. 8, pp. 1783–1804, 2016.

[14] G. B. Palmerini, "Combining thermal and visual imaging in spacecraft proximity operations," in *Control Automation Robotics & Vision (ICARCV), 13th International Conference on*. IEEE, 2014, pp. 383–388.

BIOGRAPHY
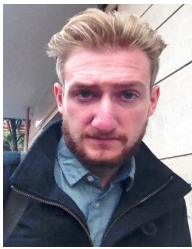
Renato Volpe *received his B.S. in Aerospace Engineering and M.Sc. in Space and Astronautical Engineering from University of Rome la Sapienza in 2016. He is currently attending a Ph.D. in Aerospace Engineering at University of Rome La Sapienza. His current research activities include GNC algorithms development and optical navigation modelling.*

Giovanni Palmerini *received his M.Sc. in Aeronautic Engineering in 1991 and a Ph.D. in Aerospace Engineering in 1996 at University of Rome La Sapienza. He is currently associate professor of Guidance and Navigation Aerospace Systems at University of Rome La Sapienza. He is Senior Member of American Institute of Aeronautics and Astronautics (AIAA).*

Christian Circi *received his M.Sc. in Aeronautic Engineering and a Ph.D. in Aerospace Engineering at University of Rome La Sapienza. He is currently researcher in Flight Mechanics and teaches Interplanetary Trajectories at University of Rome La Sapienza. His interest include trajectory optimization, low energy lunar trajectories, solar sails and launchers' ascent trajectories.*